AMERICAN METEOROLOGICAL SOCIETY

Journal of Applied Meteorology and Climatology

EARLY ONLINE RELEASE

The DOI for this manuscript is doi: 10.1175/JAMC-D-11-0215.1

Direct Radiative Effect of Mineral Dust on the Development of African Easterly Wave in Late Summer, 2003-2007

Po-Lun Ma[1,2], Kai Zhang[1], Jainn Jong Shi[3,5], Toshihisa Matsui[4,5], and Albert Arking[2],

[1]Atmospheric Sciences and Global Change Division, Pacific Northwest National Laboratory, Richland, Washington

[2]Department of Earth and Planetary Sciences, Johns Hopkins University, Baltimore, Maryland

[3]Goddard Earth Sciences and Technology Center, University of Maryland, Baltimore County, Baltimore, Maryland

[4]Earth System Science Interdisciplinary Center, University of Maryland, College Park, College Park, Maryland

[5]NASA Goddard Space Flight Center, Greenbelt, Maryland

Corresponding author: Po-Lun Ma. E-Mail: Po-Lun.Ma@pnnl.gov

Abstract

Episodic events of both Saharan dust outbreaks and African Easterly Waves (AEWs) are observed to move westward over the eastern tropical Atlantic Ocean. The relationship between the warm, dry, and dusty Saharan Air Layer (SAL) on the nearby storms has been the subject of considerable debate. In this study, the Weather Research and Forecasting (WRF) model is used to investigate the radiative effect of dust on the development of AEWs during August and September, the months of maximum tropical cyclone activity, in years 2003-2007. The simulations show that dust radiative forcing enhances the convective instability of the environment. As a result, most AEWs intensify in the presence of a dust layer. The Lorenz energy cycle analysis reveals that the dust radiative forcing enhances the condensational heating, which elevates the zonal and eddy available potential energy. In turn, available potential energy is effectively converted to eddy kinetic energy, in which local convective overturning plays the primary role. The magnitude of the intensification effect depends on the initial environmental conditions, including moisture, baroclinity, and the depth of the boundary layer. We conclude that dust radiative forcing, albeit small, serves as a catalyst to promote local convection that facilitates AEW development.

1. Introduction

Over the eastern tropical North Atlantic Ocean, episodic outbreaks of mineral dust off the African continent are observed to move westward in association with the propagation of African easterly waves (AEWs). The dust plume and the AEWs straddle the African easterly jet (AEJ) about 15°N (e.g., Karyampudi and Carlson, 1988; Karyampudi et al., 1999). The dust plume, which is embedded in the Saharan air layer (SAL)—the westward moving warm parcel of air that develops over the African continent—generally extends between 10°N and 25°N, while AEWs propagate south of the AEJ, between 5°N and 15°N. The AEWs usually have a period of 3-8 days, wavelength of 2000-4000 km, and phase speeds 6-8 m s^{-1} (e.g., Reed et al., 1977; Karyampudi and Carlson, 1988; Karyampudi et al., 1999; Zipser et al., 2009). Satellite images show convective clouds around the trough of the waves indicating the convectively active part of the AEW in association with positive relative vorticity at 700 hPa (e.g., Berry et al., 2007). The mechanism for the development of AEW was originally explained by the barotropic-baroclinic instability theory (Charney and Stern, 1962; Burpee, 1971). In recent years, Hsieh and Cook (2007; 2008) found that AEWs could be developed through the baroclinic overturning over ocean in the absence of shear instability associated with the AEJ. When environmental conditions are favorable for development, an AEW can intensify and eventually grow into a tropical cyclone (TC). It has been documented that most major hurricanes (> category 3) are originated from AEWs (Landsea, 1993).

The fact that the dust plume is often in the vicinity and at similar altitude of the vorticity center of the AEWs has generated a lot of discussions on the linkages between the SAL and the AEWs. For example, using geostationary satellite data, Dunion and Velden (2004) found that Hurricane Joyce weakened significantly right after the SAL reached Joyce while Hurricane Issac

curved northwest and avoided the SAL, and intensified into a category-4 hurricane. Evan et al. (2006) established an inverse correlation for the years 1982-2005 between atmospheric dust cover and TC activity as measured by satellite. Lau and Kim (2007) also reported an inverse correlation between the aerosol index from Ozone Monitoring Instrument and the Sea Surface Temperature (SST), suggesting that the cooler sea surface due to reduced insolation by dust could suppress TC activity. Reale et al. (2009) found that the atmospheric thermal structure associated with the SAL is unfavorable for the AEW development.

Karyampudi and Pierce (2002), on the other hand, found that the SAL had a positive impact on two of three hurricanes examined, and a negative impact on one case which was in a particularly dry year. They proposed that the SAL could increase the meridional temperature gradient, and, thus, enhance the baroclinic instability on the leading and southern edge of the SAL. The baroclinic instability can be released to facilitate further development of the disturbance. Koren et al. (2005) analyzed Moderate Resolution Imaging Spectroradiometer (MODIS) data and reached a similar finding, that the deep convection and aerosols are positively correlated. Moreover, Jones et al. (2004) found that the lower troposphere associated with the AEWs is warmed, which favors AEW intensification. They hypothesized that the dust radiative effect is responsible for such warming, corresponding to the findings in Alpert et al. (1998). Nevertheless, Braun (2010) analyzed multiple satellite datasets and found that the dust plume rarely reached the location of the disturbance to affect the AEW development. He found that the dry air responsible for suppressing TC development was a result of large-scale subsidence associated with semi-permanent high-pressure systems, and the SAL did not play a key role in this context.

Although previous observational studies have not agreed on the influence of the SAL on AEWs, numerical models have been implemented to investigate the effect of the SAL. One advantage of the modeling approach is that one can identify the effect of one factor/process of a complex system while keeping all other factors unperturbed. Many modeling studies have focused on the effect of aerosols in the SAL. The microphysical effect of aerosols on TCs has been suggested to have a negative impact on TC, but the mechanism involved is not yet conclusive. Studies show that increasing aerosols in the environment can weaken a TC by increasing the vertical wind shear (Fan et al., 2009), blocking the energy flow into the core of a storm by enhancing convection in the outer rainbands (Zhang et al., 2009; Carrio and Cotton, 2011), and diminishing convection in the core (Khain et al., 2008).

The direct radiative effect of aerosols has been found to influence the AEJ and convection in the region of interest (e.g., Tompkins et al., 2005), but its role in AEW development is not entirely clear. Lau et al. (2009) used a global GCM and found that the dust radiative effect could fashion an "elevated heat pump" mechanism (Lau and Kim, 2006) to cool the surface, warm the mid-troposphere, and create a circulation pattern that enhances subsidence over TC's main development region in the tropical North Atlantic. All of these effects are unfavorable for the development of TCs. Sun et al. (2009) found that the radiative effect of the SAL contributes to an atmospheric thermal structure that is unfavorable for AEW development. These studies are consistent with Dunion and Velden (2004), Evan el al. (2006), Lau and Kim (2007), and Reale et al. (2009). In Stephens et al. (2004), the authors found that deep convections are prohibited in the first 10 days of simulations due to dust radiative forcing. However, increased occurrence of deep convection in the dust-covered region compared with the dust-free region is observed after 10 days of simulation, which supports the observational

analysis in Koren et al. (2005), and is consistent with Karyampudi and Pierce (2002) and Jones et al. (2004).

In this study, our focus is on the direct radiative effect of aerosols on the development of AEWs, regardless of whether or not the disturbance eventually grows into a TC. Using the Weather Research and Forecasting (WRF) model, numerical experiments were conducted for 60 observed AEWs, all occurrences that lasted at least 4 days within the domain (5°N-25°N; 10°W-50°W) in August and September, in years 2003-2007. For each of the AEW cases, we conducted three simulations, one without the radiative effect of the dust, one with a dust layer located between 700 hPa and 850 hPa, and the other one with a dust layer located between 600 hPa and 850 hPa. A Lorenz energy cycle analysis (Lorenz 1955; 1967) was then applied to understand how aerosol direct radiative forcing modifies the energetics of the atmosphere and, in turn, influences the development of the AEW. In this paper, the synoptic conditions are described in Section 2. A brief description of the model is given in Section 3. Results from the numerical simulations of 60 AEWs are presented and discussed in Section 4, and conclusions are drawn in Section 5.

2. Synoptic conditions

To establish the climatology of the AEW but to avoid effects from large-scale climatic oscillation such as ENSO (El Niño-Sothern Oscillation), we limit our study to only 5 consecutive hurricane seasons, from 2003 to 2007. MODIS Aerosol Optical Thickness (AOT) was obtained from the Level 1 and Atmosphere Archive and Distribution System (http://ladsweb.nascom.nasa.gov/) at NASA/GSFC. It is Level 3 processed data, consisting of the daily average on a 1° x 1° latitude-longitude grid of the 10 km x 10 km retrievals from the

MODIS sensor on the Terra satellite (Remer et al., 2005). Relative vorticty, winds, and temperature were obtained from the ECMWF operational analysis for the same period. For comparison with MODIS observations, we use only the 12Z ECMWF data, in order to maximize alignment with the Terra satellite, which passes over the eastern tropical North Atlantic Ocean in the late morning.

The data shows that in the boreal summer, the strongest easterly wind, which defines the AEJ, is observed at about 15°N (Figure 1, left panel). In the meantime, positive relative vorticity, which indicates the vorticity field of the background flow as well as the trough of the AEWs, are in the area south of the AEJ and south of the dust plume, which is north of the AEJ. Relative vorticity is strongest near the coast of Africa, and its magnitude gradually decreases as the AEWs propagate westward. The dust layer extends appreciably from 10°N to 25°N and spreads up to around 40 degrees west of the African coast, with a maximum close to the coast. As the dust plume travels westward, AOT decreases due to settling on the ocean surface. Regarding inter-annual variability, the dust plume is the most opaque and extends the farthest in 2003, and the least opaque in 2007.

The AEWs poleward of 15°N are dominated by the relative vorticity field at 850 hPa and AEWs equatorward of 15°N are dominated by 600 hPa relative vorticity (Thorncroft and Hodges, 2001). Following the work by Berry et al. (2007), we chose 700 hPa to analyze the AEWs in this study. The temperature and winds at 700 hPa (Figure 1, middle panel) shows that the warm air to the north and the cool air to the south, straddling the AEJ at about 15°N, result in horizontal wind shear about the AEJ. The anti-cyclonic circulation associated with the warm air parcel indicates a convectively stable condition with subsidence in the area. Due to the thermal wind relation, the strongest easterlies are found at about 700 hPa. The warm air extends to about

40°W in most years, except in 2004, when the warm air was confined mostly east of 20°W. The meridional temperature gradient is about 4 K over 20 degrees of latitude over land and only about 1 K over ocean at 30 °W. At about 40°W, where the environmental shear instability vanishes, baroclinic overturning could reverse the sign of the gradient of meridional potential vorticity and thus provide instability (Hsieh and Cook, 2007; 2008). The meridional temperature gradient at 1000 hPa (Figure 1, right panel) varies from 16 K per 20 degrees over land (at 5 °W) to -2 K over ocean, where the air temperature near the surface is strongly affected by the SST. The data shows that the warm air associated with the SAL is elevated in altitude and does not extend to the surface.

In Figure 2, the time series of 700 hPa relative vorticity and AOT, averaged between 15°W and 50°W, shows that the strong relative vorticity to the south is often accompanied with high AOT to the north. The correlation coefficient between the time series of AOT averaged over the north part of the domain and the time series of relative vorticity averaged over the south part of the domain is 0.34. TC-genesis often occurs at the southern edge of the dust plume and the northern edge of the vorticity field of the background flow. Furthermore, The amplitude and latitudinal positions of maximum AOT and relative vorticity vary with season in tandem. In June and October, the dust plume and the AEW are in further south than in July, August, and September. Both dust and AEW activity are generally calm in October, when TC-genesis is less frequent. The dust outbreaks are stronger and more frequent in the early months than in the latter months of a hurricane season, except for 2005, in which the dust outbreak events took place mostly from July to mid-September. These features are also discussed in previous studies (e.g., Calrson and Prospero, 1972; Dunion, 2011). On the other hand, the AEW tends to be weaker in June, July, and October, and stronger in August and September. Although one would expect a

more intense disturbance to have a better chance of becoming a TC, not every intense AEW disturbance reaches that stage. More TCs are developed in 2003, 2004, and 2005 than in 2006 and 2007, despite the fact that the number of AEWs and dust outbreaks did not change much (Table 1).

Since most TCs occur in late summer, we limited the period for the numerical simulations to August and September, and identified a total of 60 AEW disturbances over the 5-year period. There was only one criterion for selection, viz., the AEW last at least 4 days. The 700 hPa relative vorticity of the AEW must be larger than $1 \times 10^{-5}\ s^{-1}$ for at least four days within this domain in order to be considered in this study. The dates that the AEWs leave the coast of Africa are shown in Table 2. As one can see in Figure 3, on average, the vorticity center of the AEWs moves about 6 degrees westward per day. The AEWs weaken as they propagate further west. The dust plumes are generally found in the northern periphery of the vortices. Although the major part of the dust layer lies north of the vortex, it can extend as far south as the vortex center and even beyond. Figure 3 shows that part of the dust plume gradually extends from north to west of the vorticity center, counter-clockwisely in accordance with the drift of the vortices. The southern edge of the dust plumes can extend to about 8 °N, about 5 degrees further south to the composite vorticity center. The synoptic conditions of the AEWs and the associated dust layer in the 5 late summers are similar to previous observational studies and will be used as we construct our numerical experiments.

It is worth noting that MODIS AOT is not derived in cloudy areas and convective clouds associated with AEWs (Berry et al., 2007) can obscure the AOT retrieval. Hence, the dust plume in the real-atmosphere can be even closer to the vorticity center (i.e., further south) because of the bias inherent in the AOT retrieval.

3. Model description

The WRF Version 3.1.1 is used to investigate the direct radiative effect of dust on the AEW. We implemented in WRF the NASA/GSFC (National Aeronautics and Space Administration/Goddard Space Flight Center) radiative transfer model (Chou and Suarez, 1999; 2001) with recent improved features (Matsui et al., 2007; as described in Shi et al., 2010). In this configuration, aerosol radiative properties are part of the input to the radiative transfer model, along with temperature and the radiative properties of the gaseous atmosphere, so that the aerosol radiative forcing is included in the radiative heating rate calculation. The non-radiative effects of aerosols (e.g., hydrological or mechanical) are not included in the model for this study and are beyond the scope of this paper.

The physical parameterizations selected for the model runs are the Goddard microphysics scheme (Tao and Simpson, 1993; Tao et al., 2003), Kain-Fritsch cumulus scheme (Kain, 2004), Yonsei University planetary boundary layer (PBL) scheme (Hong et al., 2006), and Noah land-surface scheme (Chen and Dudhia, 2001). For initial and boundary conditions, we use the ECMWF (European Centre for Medium-Range Weather Forecasts) advanced operational analysis, obtained from the ECMWF Data Server (http://www.ecmwf.int/products/data/archive/index.html). The gridded analysis dataset presents the AEW reasonably and has been used to study the AEWs (e.g., Reed et al., 1988; Thorncroft and Hodges, 2001).

It is worth noting that the warming or cooling of air by absorption and emission of radiation energy is instantaneous, while warming or cooling of the sea surface occurs on a much longer time scale due to the latency in ocean response (e.g., Arking and Ziskin, 1994). Hence, in our model, the sea surface temperature (SST) is not affected by direct radiative effect of aerosols.

However, in the time scale shorter than a few days, SST is a function of wind speed. While strong surface winds are expected in the presence of an AEW or TC, storm-forced SST cooling (Price, 1981; Sanford et al., 1987) can weaken the parent (Black and Holland, 1995) and the future storms (Brand, 1971). In our simulations, we use ECMWF operational analysis, which has assimilated observational data and contains both SST and winds, as our initial and boundary conditions. The model calculates the meteorological fields within the domain. However, the SST, as the lower boundary condition, is not affected by the simulated meteorological fields. Therefore, the instantaneous response of SST to the high surface winds associated with the storm cannot be captured in our model and is beyond the scope of this study.

The model grid is 300 (east-west) by 180 (north-south) by 24 (vertical), covering the eastern tropical North Atlantic Ocean where the AEW and the dust-laden SAL that develop over the African continent move generally westward in this region. The projection method used to create the domain is Lambert conformal conic projection with the two intersecting true latitudes being 10°N and 20°N, and the center point 15°N, 30°W. The corner points of the domain are: southwest 2.15°N, 49.72°W; southeast 2.15°N, 10.28°W; northwest 25.98°N, 52.07°W; northeast 25.98°N, 7.93°W. The horizontal grid spacing is 15 km.

In this study, our goal is to understand the radiative effect of mineral dust on the AEWs, not the model's ability simulating a dust plume. The aerosol radiative properties depend on aerosols' physical and chemical properties such as size distribution, mass, composition, etc., as well as the conversion from aerosol's physical and chemical properties to the radiative properties in the model such as refractive indices assumed and the averaging rule adopted (Fast et al., 2005; Barnard et al., 2010). Accurately simulating aerosol's mass, number, and size distribution that involves complex processes such as the mobilization, transport, and deposition of mineral dust

remains a difficult task. As a result, the large uncertainty associated with the dust direct radiative forcing can lead to a different impact upon the climate system (Zhao et al., 2010). These uncertainties require further investigations and are beyond the scope of this study. While acknowledging the fact that there exist large uncertainties associated with the radiative property as well as the distribution of Saharan dust, we focus on the atmospheric response (i.e., the intensification of AEWs) to a prescribed dust layer, which has the properties and distribution within the range of reported dust events.

For each of the 60 AEW cases (Table 2), we conduct three 6-day simulations, the control experiment of "no aerosol" (NA), a "with aerosol" (WA) experiment with a prescribed dust plume located at lower altitudes (WA_L), and a WA experiment with a prescribed dust plume extends to higher altitudes (WA_H). The dust layer is placed to the north of 15 °N, in accordance with the observation (Figure 3). One limitation of this prescribed dust layer is that the transport and removal processes of aerosols are ignored. The prescribed dust layer exerts the same radiative forcing constantly throughout the entire simulation period, resulting in a continuous forcing that gradually builds up its effect on the AEW and the environment. In the real atmosphere, mineral dust can be gradually removed from the atmosphere through dry deposition and wet scavenging as the dust plume moves further west into the Atlantic Ocean, as shown in Figure 3. As a result, its radiative forcing is expected to be the strongest when the AEW and the dust plume are close to the coast of the African continent, and fade away over time. For vertical distribution, dust aerosols are evenly distributed between 700 hPa and 850 hPa for WA_L, corresponding to the high scattering layer between 1.2 km and 3 km during a vertical descent through the SAL reported in Zipser et al. (2009). For WA_H experiments, the dust layer is placed between 600 hPa and 850 hPa, similar to the vertical distribution reported in Myhre et al. (2003).

The radiative properties of the dust layer are set in accordance with values in previous studies. For optical thickness, we set the shortwave AOT (τ^{sw}) to 1.0, which is about 30% less than what Haywood et al. (2003) reported in an event with the heaviest dust loading (τ^{sw} = 1.5). The longwave AOT (τ^{lw}) is set to 0.5, half of the τ^{sw}, as suggested in Haywood et al. (2005) while using the refractive index from Volz (1973). Note that because we prescribed the radiative properties of aerosols (optical thickness, single scattering albedo, and asymmetry factor), the refractive index is not directly used in our calculations. However, it is important to acknowledge that using different refractive indices gives very different longwave-to-shortwave (IR-to-VIS) AOT ratio. Refractive index depends on the composition of dust particles. The refractive index used in climate models is often based on World Climate Program (WCP, 1986) or Volz (1972). Fouquart et al. (1987) used measurements of Saharan dust over Niger for estimating refractive index. In Haywood et al. (2005), the authors reported that the IR-to-VIS AOT ratio is 0.33 while using the refractive index in Fouquart et al. (1987), and 0.52 while using the refractive index in Volz (1972). Highwood et al. (2003) stated that the as AOT at 0.55 micron is 0.67, AOT at 10 micron varies from 0.4 to 0.23 when different refractive index is used, rendering the IR-to-VIS AOT ratio ranges from about 0.60 to 0.34. In Hansell et al. (2010), the authors reported IR-to-VIS AOT ratio as high as 0.75 occasionally, but adopted the refractive index in Volz (1972) for their radiative transfer calculation because their focused area is around Cape Verde of which the mineralogy of dust particles is similar to that in Volz (1972). In our study, we adopted the IR-to-VIS AOT ratio estimated from using the refractive index in Volz (1972) also because our focused domain is the eastern tropical North Atlantic Ocean. For single scattering albedo in the shortwave bands (ω_0^{sw}), Forster et al. (2007) documented that the SSA for dust reported from various studies ranges from 0.90 to 0.99, with a median value of 0.96. In Myhre et al. (2003),

the observed SSA near Cape Verde is about 0.96-0.97. In this study, we set the SSA = 0.96. Other radiative properties including longwave single scattering albedo (ω_0^{lw}) as well as asymmetry factor in shortwave (g^{sw}) and longwave (g^{lw}) bands are set to values within the range reported in Dufresne et al. (2002) and Haywood et al. (2005). The complete list of settings for the prescribed dust radiative properties is given in Table 3.

4. Numerical simulations for 60 AEWs

Using a stand-alone NASA/GSFC radiative transfer model (Chou and Suarez, 1999; 2001), we found that the maximum radiative forcing exerted by the prescribed dust layer occurs at local noon. The instantaneous shortwave aerosol radiative forcing for both WA_L and WA_H is about -140 W m^{-2} at surface and -82 W m^{-2} at top-of-atmosphere (TOA). The longwave radiative forcing at surface is 28 W m^{-2} for WA_L and 26 W m^{-2} for WA_H; at TOA, 8 W m^{-2} for WA_L and 11 W m^{-2} for WA_H. As shown in Figure 4a, when the dust layer is placed between 700 hPa and 850 hPa, the atmospheric temperature profile can be modified. The decrease in the net solar radiative flux, due to scattering, causes a net cooling of the air column below the dust layer by about 0.3 K day^{-1}. Within the dust layer, the reduction in insolation is overtaken by absorption of solar radiation within the layer, resulting in a 3 K day^{-1} heating. On the other hand, dust longwave radiative forcing traps the terrestrial radiation and causes a warming of the air column below the dust layer by about 1.4 K day^{-1}. Within the dust layer, the dust aerosols cause a cooling effect due to longwave emission. As a result, at local noon, the prescribed dust layer causes a net 2 K day^{-1} warming in the dust layer, and about a 1 K day^{-1} warming for the air column below the layer. In Figure 4b, the dust-induced heating/cooling in the WA_H configuration is slightly weaker and extends to higher altitudes than that the WA_L configuration,

but the main characteristics are the same. Note that daily averaged dust-induced heating rate can be much smaller than the instantaneous dust-induced heating rate at local noon. The heating rate computed from our model is about the same magnitude to the heating rate computed in Carlson and Benjamin (1980), in which the authors reported that the daily mean shortwave clear-sky dust radiative heating rate within the dust layer for AOT = 1.0 is about 2 K day^{-1}. Instantaneous clear-sky dust heating rate can be as large as 5 K day^{-1} as reported in Mallet et al. (2009) and Lemaître et al. (2010), but long-term dust-induced heating rate climatology can be much smaller (Evan and Mukopadhyay, 2010). In addition, as aforementioned, uncertainties associated with dust radiative properties can result in different heating rate profiles. For example, Wong et al. (2009) reported that their heating rate is smaller than Carlson and Benjamin (1980), possibly due to different mineralogy and size distribution assumed in the model.

As a result of the aerosol radiative forcing, the atmospheric temperature profile in the model can be significantly altered, as shown in Figure 5. Comparing the WA_L and NA experiments (Figure 5a), the dust-induced heating causes the lower troposphere to warm by about 0.3-0.5 K below the dust layer and about the 0.2-0.4 K cooling within the dust layer, with an appreciable diurnal cycle. WA_H experiments show a similar but weaker effect, about 0.2-0.4 warming below the dust layer and 0.1-0.3 cooling within the dust layer (Figure 5b). The diurnal cycle of the temperature difference is due to the fact that aerosol shortwave radiative forcing follows the diurnal cycle of the solar irradiance. The fact that the magnitude of the temperature difference in Figure 5 is much smaller than the magnitude of the aerosol radiative heating rate in Figure 4 suggests a much smaller dust-induced heating/cooling over a day, compared with instantaneous heating at local noon (Figure 4), and a possible rapid adjustment of the temperature field by convection and circulation. Moreover, as shown in Figure 6, the alteration

of the temperature profile decreases convective stability after 24 hours of simulation for model spin-up. The decrease of convective stability is attributed to the warming of the lower troposphere. The magnitude of the tropospheric stability difference ranges from -0.1 K to -0.6 K with a diurnal cycle corresponding to that of the temperature difference. The change of temperature in the lower troposphere provides a favorable condition for shallow convection, which facilitates vertical mixing in the lower troposphere. As a result, the convective available potential energy (CAPE) over the domain increases by about 20%, from an average of 824 J kg^{-1} for all the NA experiments to 1002 J kg^{-1} for the WA_L and 1009 J kg^{-1} for WA_H experiments. Hence, the isentropic surface is elevated in the WA experiments, and that causes the lower-tropospheric isentropic potential vorticity to increase for most cases (Figure 7). It is worth noting that the increase of CAPE in this study is the result of the radiative effect of the prescribed dust layer. While the thermal structure of the SAL, which is already embedded in the initial and boundary conditions in the simulations, can decrease CAPE and prohibit convections (Dunion, 2011), our results suggest that the dust-induced change of atmospheric temperature profile can counteract the effect of the SAL on modifying CAPE.

To further understand the physical mechanism, we compute the Lorenz energy cycle (Lorenz 1955; 1967), which was originally developed to analyze the energetics of the global atmospheric circulation but has also been applied to analyze AEW disturbances (e.g., Karyampudi and Carlson, 1988; Hsieh and Cook 2007). Following the formulations in Hsieh and Cook (2007), we compute for the total atmospheric column (from surface to 100 hPa) the zonal available potential energy (P_Z), zonal kinetic energy (K_Z), eddy available potential energy (P_E), and eddy kinetic energy (K_E). We also calculate the energy conversion rate between P_Z and P_E (C_A), energy conversion rate between K_Z and K_E (C_K), energy conversion rate between P_E and

K_E (C_{PK}), and energy conversion rate between P_Z and K_Z (C_z). Finally, we compute the effective diabatic heating that produces P_Z due to condensational heating (H_Z^C), the effective diabatic heating that produces P_Z due to radiative heating (H_Z^R), the effective diabatic heating that produces P_Z due to PBL scheme heating (H_Z^B), the effective diabatic heating that produces P_E due to condensational heating (H_E^C), the effective diabatic heating that produces P_E due to radiative heating (H_E^R), and the effective diabatic heating that produces P_E due to PBL scheme heating (H_E^B). For this calculation, we took the domain-average and discard the data from the first day of the simulations when the model is in the spin-up process and average the results between the 2nd and last day of the simulation for all NA and WA simulations.

In the 60 sets of simulations, we observe that the occurrence of stronger storms increases (Figure 8). The frequency of occurring the weakest AEWs, K_E less than 100 kJ, decreases 35 % in the WA_L and 25% in WA_H experiments, while the occurrence of the strongest AEWs remains the same. In Figure 9, it appears that the dust direct radiative forcing in WA_L enhances 57 out of 60 AEWs, ranging from a few percent to about 30 percent. In WA_H experiments, 58 out of 60 AEWs are intensified. However, the intensification in the WA_H experiments is weaker than the WA_L experiments. Furthermore, the AEWs intensify more rapidly over time (Figure not shown) as the dust radiative effect continuously builds up.

The Lorenz energy cycle also reveals the physical processes involved in the intensification of AEWs. As shown in Table 4, except for C_A which slightly decreases, the other 3 energy conversion rates increase. In particular, the 5.6% (5.1%) increase of eddy kinetic energy in WA_L (WA_H) experiments is directly attributed to, first and foremost, the enhanced conversion between the eddy available potential energy and the eddy kinetic energy, which increases 0.09 (0.063) W m^{-2}, about a 27% (19%) increase. The energy conversion between the

zonal kinetic energy and the eddy kinetic energy in WA_L (WA_H) experiments increases about 0.01 (0.016) W m^{-2}. Furthermore, the diabatic heating terms suggest that the condensational heating is the primary energy source. The radiative heating plays a minor role and has a negative effect on the energy terms. This can be explained by the fact that as the storm gets intensified, the cloudy area expands and thus the cloud-radiation feedback causes a cooling effect on the atmosphere. As shown in Table 4, we think that the dust direct radiative forcing, albeit small, serves as a catalyst that destabilizes the atmosphere and facilitates convections. The increased cloud cover associated with the enhanced convections causes a negative feedback through radiation, but it is very small compared with the additional condensational heating released from the convections. The additional condensational heating increases available potential energy for both zonal mean flow and the eddy. In turn, the available potential energy is effectively converted to elevate the kinetic energy of the zonal mean flow and the eddy. The kinetic energy of the zonal mean flow can then be converted to increase the eddy kinetic energy. Among the 4 energy conversion terms, we find that the local convective overturning plays the primary role to increase the eddy kinetic energy by converting the eddy available potential energy.

It is interesting that the energy intensification due to the same aerosol radiative forcing varies and depends upon the particular character of each AEW. To determine which factors play a role, we examined the correlation of the intensification ($\Delta K_E = K_E^{WA} - K_E^{NA}$) with respect to environmental conditions typically considered as important factors for cyclogensis, such as SST, 600 hPa relative humidity, CAPE, PBL height (H_{PBL}), vertical wind shear between 200 and 850 hPa ($\vec{V}_{shr}$), total column precipitable water (Q_{column}), vertical temperature gradient, the initial strength of the eddy, etc. Among these variables, we found that the increase of eddy kinetic energy is significantly correlated with precipitable water (R = 0.50), vertical wind shear between

200 mb and 850 mb (R = 0.51), and PBL height (R = 0.49), for the WA_L configuration. The multivariate regression model has the form:

$$\Delta K_E = 0.05Q_{column} + 0.97\vec{V}_{shr} + 0.03H_{PBL} - 115.8 ,$$

with the R-squared value equals 0.46. Other variables aforementioned are also moderately correlated with ΔK_E with a correlation coefficient about or larger than 0.4, but they do not pass Student's t-test with a significance level = 0.05 on top of the 3 variables. For WA_H configuration, we found that the increase of eddy kinetic energy is significantly correlated with precipitable water (R = 0.49) and PBL height (R = 0.46), and the multivariate regression model has the form:

$$\Delta K_E = 0.05Q_{column} + 0.03H_{PBL} - 107.6 ,$$

with the R-squared value equals 0.36. It should be noted that the development of AEWs depends on the environmental conditions as well as the interaction between the AEW and the environment, which can vary case by case. The dust-induced intensification in this study is found to be associated with enhanced local convective overturning. Thus, when the dust radiative forcing fortifies the original environmental conditions to facilitate local convective overturning, the dust-induced intensification is found the most evident. From the multivariate regression model, it is suggested that when the environment is moist and has an unstable PBL, which contribute to convective instability, the dust radiative forcing is likely to intensify the AEW more effectively. For the WA_L experiments, the larger baroclinicity, which is associated with the north-to-south temperature gradient, can also contribute to larger intensification of AEWs since the dust-induced heating further enhances the horizontal temperature gradient. In WA_H experiments, vertical wind shear was also well-correlated with the increase of eddy kinetic

energy (R=0.41), but it did not pass the significant test to be included in the regression model on top of precipitable water and PBL height.

5. Conclusions

In this study, we performed a large number of numerical simulations to explore the possible role of radiative forcing by mineral dust in intensifying AEWs. While acknowledging the large uncertainty associated with the radiative properties and distribution of dust aerosols, we applied prescribed dust layers in the model with radiative properties and distributions within the range reported in previous studies. The simplified dust layer helps us to isolate the direct radiative effect of dust on the AEW development from non-linear responses of the aerosol-meteorology interaction in a model that fully couples the aerosols, clouds, radiative transfer, and circulation.

Despite the uncertainties associated with mineral dust, the large number of simulations using prescribed simple dust layers establishes the statistical validity of the radiative effect of the dust layer on the intensification of AEWs. We found that dust radiative forcing modifies the vertical temperature profile by warming the lower tropopsphere and thereby decreases atmospheric stability. As stability decreases, most AEWs intensify. The model results are consistent with the observational studies of Alpert et al. (1998) and Jones et al. (2004). Furthermore, the Lorenz energy cycle analysis suggests that in the presence of a dust layer, the condensational heating increases dramatically and is effectively converted to eddy kinetic energy through convective overturning. The magnitude of intensification varies from one AEW to another and is the strongest when the environment is characterized as moist, baroclinic, and has a higher PBL.

Acknowledgement

We thank the three anonymous reviewers for their insightful comments. We thank William K.-M. Lau, Darryn Waugh, Ming-Dah Chou, Wei-Kuo Tao, Milton Halem, Lorrain Remer, and Yoram Kaufman for helpful discussions. We thank Dave Strenski, Norman Barnhart, and Peter Johnsen at Cray Inc., for providing access to and help with the Cray XT5 supercomputer. We thank De-Iou Tsai for his help with scripts for running the model and Chun-Chi Lien for her help obtaining the ECMWF data. This study is supported by Department of Earth and Planetary Sciences, Johns Hopkins University, and is supported by Multicore Computational Center at University of Maryland, Baltimore County. This study is supported by the Office of Science (BER), U. S. Department of Energy. The Pacific Northwest National Laboratory is operated for DOE by Battelle Memorial Institute under contract DE-AC06-76RLO 1830.

References

Alpert, P., Y. J. Kaufman, Y. Shay-El, and coauthors, 1998: Quantification of dust- forced heating of the lower troposphere, *Nature*, **395**, 367–370.

Arking, A. and D. Ziskin, 1994: Relationship between clouds and sea surface temperatures in the western tropical Pacific. *J. Climate*, **7**: 988–1000.

Barnard, J.C., J.D. Fast, G. Paredes-Miranda, W.P. Arnott, and A. Laskin, 2010: Technical note: evaluation of the WRF-Chem "aerosol chemical to aerosol optical properties" module using data from the MILAGRO campaign, *Atmos. Chem. Phys.*, **10**, 7325-7340, doi:10.5194/acp-10-7325-2010.

Berry, G., C. Thorncroft, and T. Hewson, 2007: African Easterly Waves during 2004—Analysis Using Objective Techniques. *Mon. Wea. Rev.*, **135**: 1251–1267.

Black, P. G., and G. J. Holland, 1995: The boundary layer of tropical Cyclone Kerry (1979), *Mon. Weather Rev*., **123**, 2007–2028.

Brand, S., 1971: The effects on a tropical cyclone of cooler surface waters due to upwelling and mixing produced by a prior tropical cyclone, *J. Appl. Meteorol*., **10**, 865–874.

Braun, S. A., 2010: Reevaluating the Role of the Saharan Air Layer in Atlantic Tropical Cyclogenesis and Evolution. *Mon. Wea. Rev.*, **138**, 2007–2037. doi: 10.1175/2009MWR3135.1.

Burpee, R., 1972: The Origin and Structure of Easterly Waves in the Lower Troposphere of North Africa. *J. Atmos. Sci*., **29**: 77–90.

Carlson, T. N. and J. M. Prospero, 1972: The large-scale movement of Saharan air outbreaks over the northern equatorial Atlantic. *J. Appl. Meteor.,* **11,** 283-297.

Carlson, T. N., and S. G. Benjamin, 1980: Radiative heating rates for Saharan dust. *J. Atmos. Sci.,* **37,** 193–213.

Carrio, G. G. and W. R. Cotton, 2011: Investigations of aerosol impacts on hurricanes: virtual seeding flights, *Atmos. Chem. Phys*., **11**, 2557-2567, doi:10.5194/acp-11-2557-2011.

Charney, J., and M. Stern, 1962: On the Stability of Internal Baroclinic Jets in a Rotating Atmosphere. *J. Atmos. Sci.,* **19**: 159–172.

Chen, F., and J. Dudhia, 2001: Coupling an advanced land-surface/ hydrology model with the Penn State/ NCAR MM5 modeling system. Part I: Model description and implementation. *Mon. Wea. Rev.*, **129**: 569–585.

Chou, M.-D., and M. J. Suarez, 1999: A solar radiation parameterization for atmospheric studies, *NASA Tech. Memo*., *NASA-TM-1999-104606*, vol. **15**, 40 pp.

Chou M.-D., and M. J. Suarez, 2001: A thermal infrared radiation parameterization for atmospheric studies. *NASA/TM-2001-104606*, vol. **19**, 55pp.

Dufresne, Jean-Louis, Catherine Gautier, Paul Ricchiazzi, Yves Fouquart, 2002: Longwave Scattering Effects of Mineral Aerosols. *J. Atmos. Sci.*, **59**, 1959–1966.

Dunion, J. P. and C. S. Velden, 2004: The Impact of the Saharan air layer on Atlantic tropical cyclone activity. *Bull. Amer. Meteor. Soc.*, **85**: 353-365.

Dunion, J. P., 2011: Rewriting the Climatology of the Tropical North Atlantic and Caribbean Sea Atmosphere. *J. Climate*, **24**, 893–908.

Evan, A. T., J. Dunion, J. A. Foley, A. K. Heidinger, and C. S. Velden, 2006: New evidence for a relationship between Atlantic tropical cyclone activity and African dust outbreaks, *Geophys. Res. Lett*., **33**: L19813, doi:10.1029/2006GL026408.

Evan, A. T. and S. Mukhopadhyay, 2010: African Dust over the Northern Tropical Atlantic: 1955–2008. *J. Appl. Meteor. Climatol.*, **49**, 2213–2229, doi: 10.1175/2010JAMC2485.1.

Fan, J., T. Yuan, J. M. Comstock, S. Ghan, A. Khain, L. R. Leung, Z. Li, V. J. Martins, and M. Ovchinnikov, 2009: Dominant role by vertical wind shear in regulating aerosol effects on deep convective clouds, *J. Geophys. Res.*, **114**: D22206, doi:10.1029/2009JD012352.

Fast, J.D., W.I. Gustafson Jr., R.C. Easter, R.A. Zaveri, J.C. Barnard, E.G. Chapman, G.A. Grell, and S.E. Peckham, 2005: Evolution of ozone, particulates, and aerosol direct radiative forcing in the vicinity of Houston using a fully-coupled meteorology-chemistry-aerosol model. *J. Geophys. Res.*, **111**, doi:10.1029/2005JD006721.

Forster, P., V. Ramaswamy, P. Artaxo, T. Berntsen, R. Betts, D.W. Fahey, J. Haywood, J. Lean, D.C. Lowe, G. Myhre, J. Nganga, R. Prinn, G. Raga, M. Schulz and R. Van Dorland, 2007: Changes in Atmospheric Constituents and in Radiative Forcing. *In: Climate Change 2007: The Physical Science Basis. Contribution of Working Group I to the Fourth Assessment Report of the Intergovernmental Panel on Climate Change* [Solomon, S., D. Qin, M. Manning, Z. Chen, M. Marquis, K.B. Averyt, M.Tignor and H.L. Miller (eds.)]. Cambridge University Press, Cambridge, United Kingdom and New York, NY, USA.

Fouquart, Y., B. Bonnel, G. Brogniez, J. C. Buriez, L. Smith, J. J. Morcrette, and A. Cerf, 1987: Observations of Saharan aerosols: Results of ECLATS field experiment. Part II: Broadband radiative characteristics of the aerosols and vertical radiative flux divergence. *J. Climate Appl. Meteor.*, **26**, 38–52.

Hansell, R. A., S.-C. Tsay, Q. Ji, N. C. Hsu, M.-J. Jeong, S. H. Wang, K. N. Liou, and S. C. Ou (2009), An assessment of surface longwave direct radiative effect of airborne saharan

dust during the NAMMA field campaign, *J. Atmos. Sci.*, **67(4)**, 1048–1065, doi:10.1175/2009JAS3257.1.

Haywood, J., P. Francis, S. Osborne, M. Glew, N. Loeb, E. Highwood, D. Tanre, G. Myhre, P. Formenti, and E. Hirst, 2003: Radiative properties and direct radiative effect of Saharan dust measured by the C-130 aircraft during SHADE: 1. Solar spectrum. *J. Geophys. Res.*, **108**(D18): 8577, doi:10.1029/2002JD002687.

Haywood, J. M., R. P. Allan, I. Culverwell, T. Slingo, S. Milton, J. Edwards, and N. Clerbaux (2005), Can desert dust explain the outgoing longwave radiation anomaly over the Sahara during July 2003, *J. Geophys. Res*., **110**, D05105, doi:10.1029/2004JD005232.

Highwood, E. J., J. M. Haywood, M. D. Silverstone, S.M. Newman, and J. P. Taylor (2003): Radiative properties and direct effect of Saharan dust measured by the C-130 aircraft during Saharan Dust Experiment (SHADE): 2. Terrestrial spectrum. *J. Geophys. Res.*, **108**, 8578, doi:10.1029/2002JD002552.

Hong, S.-Y., Noh, and J. Dudhia, 2006: A new vertical diffusion package with an explicit treatment of entrainment processes. *Mon. Wea. Rev*., **134**, 2318–2341.

Hsieh, J-S. and K. H. Cook, 2007: A study of the energetics of African easterly waves using a regional climate model. *J. Atmos. Sci*., **64**: 421–440.

Hsieh, J.S., and K.H. Cook, 2008: On the Instability of the African Easterly Jet and the Generation of African Waves: Reversals of the Potential Vorticity Gradient. *J. Atmos. Sci*., **65**, 2130–2151.

Jones, C., N. Mahowald, and C. Luo (2004), Observational evidence of African desert dust intensification of easterly waves, *Geophys. Res. Lett*., **31**, L17208, doi:10.1029/ 2004GL020107.

Kain, J. S., 2004: The Kain-Fritsch convective parameterization: An update. *J. Appl. Meteor*., **43**, 170–181.

Karyampudi, V.M., and T.N. Carlson, 1988: Analysis and Numerical Simulations of the Saharan Air Layer and Its Effect on Easterly Wave Disturbances. *J. Atmos. Sci*., **45**: 3102–3136.

Karyampudi, V.M., S.P. Palm, J.A. Reagen, H. Fang, W.B. Grant, R.M. Hoff, C. Moulin, H.F. Pierce, O. Torres, E.V. Browell, and S.H. Melfi, 1999: Validation of the Saharan Dust Plume Conceptual Model Using Lidar, Meteosat, and ECMWF Data. *Bull. Amer. Meteor. Soc*., **80**: 1045–1075.

Karyampudi, V.M., and H.F. Pierce, 2002: Synoptic-Scale Influence of the Saharan Air Layer on Tropical Cyclogenesis over the Eastern Atlantic. *Mon. Wea. Rev*., **130**: 3100–3128.

Khain, A., N. Cohen, B. Lynn, A. Pokrovsky, 2008: Possible Aerosol Effects on Lightning Activity and Structure of Hurricanes. *J. Atmos. Sci.*, **65**, 3652–3677. doi: 10.1175/2008JAS2678.1

Koren, I., Y. J. Kaufman, D. Rosenfeld, L. A. Remer, and Y. Rudich, 2005: Aerosol invigoration and restructuring of Atlantic convective clouds, *Geophys. Res. Lett.*, **32**: L14828, doi:10.1029/2005GL023187.

Landsea, C.W., 1993: A climatology of intense (or major) Atlantic hurricanes. *Mon. Wea. Rev*., **121**: 1703-1713.

Lau, K.-M. and K.-M. Kim, 2006: Observational relationships between aerosol and Asian monsoon rainfall, and circulation, *Geophys. Res. Lett.*, **33**: L21810, doi:10.1029/2006GL027546.

Lau, W. K.M., and K.-M. Kim, 2007: How Nature Foiled the 2006 Hurricane Forecasts, *Eos Trans. AGU*, **88**(9**)**, doi:10.1029/2007EO090002.

Lau, K. M., K. M. Kim, Y. C. Sud, and G. K. Walker, 2009: A GCM study of the response of the atmospheric water cycle of West Africa and the Atlantic to Saharan dust radiative forcing. *Ann. Geophys.*, **27**: 4023-4037.

Lemaître, C., Flamant, C., Cuesta, J., Raut, J.-C., Chazette, P., Formenti, P., and J. Pelon (2010): Radiative heating rates profiles associated with a springtime case of Bodélé and Sudan dust transport over West Africa, *Atmos. Chem. Phys.*, **10**, 8131-8150, doi:10.5194/acp-10-8131-2010.

Lorenz, E. N., 1955: Available potential energy and the maintenance of the general circulation. *Tellus,* **7**: 157–167.

Lorenz E. N., 1967: *The Nature and Theory of the General Circulation of the Atmosphere*. World Meteorological Organization: Geneva; No. 161.

Mallet, M., Tulet, P., Serça, D., Solmon, F., Dubovik, O., Pelon, J., Pont, V., and O. Thouron (2009): Impact of dust aerosols on the radiative budget, surface heat fluxes, heating rate profiles and convective activity over West Africa during March 2006, *Atmos. Chem. Phys.*, **9**, 7143-7160, doi:10.5194/acp-9-7143-2009.

Matsui, T., W-K. Tao, and R. Shi, 2007: Goddard radiation and aerosol direct effect in Goddard WRF. *NASA/UMD WRF Workshop,* College Park, Maryland, NASA and University of Maryland, College Park, 12 pp. [Available online at http://www.atmos.umd.edu/~martini/wrfchem/ppt/WRF_Toshi.ppt].

Myhre, G., A. Grini, J. M. Haywood, F. Stordal, B. Chatenet, D. Tanre´, J. K. Sundet, and I. S. A. Isaksen (2003), Modeling the radiative impact of mineral dust during the Saharan Dust Experiment (SHADE) campaign, *J. Geophys. Res.*, **108(D18)**, 8579, doi:10.1029/2002JD002566

Price, J. F., 1981: Upper ocean response to a hurricane, *J. Phys. Oceanogr*., **11**, 153–175.

Reale, O., W. K. Lau, K-M. Kim, and E. Brin, 2009: Atlantic tropical cyclogenetic processes during SOP-3 NAMMA in the GEOS-5 global data assimilation and forecast system. *J. Atmos. Sci.*, **66,** 3563–3578.

Reed, R.J., D.C. Norquist, and E.E. Recker, 1977: The Structure and Properties of African Wave Disturbances as Observed During Phase III of GATE. *Mon. Wea. Rev.,* **105**: 317–333.

Reed, R J, E Klinker, and A. Hollingsworth, 1988: The structure and characteristics of African easterly wave disturbances determined from ECMWF operational analysis/forecast system. *Meteorol. Atmos. Phys.,* **38**: 22–33.

Remer, L. A., Y. J. Kaufman, D. Tanré, S. Mattoo, D. A. Chu, J. V. Martins, R.-R. Li, C. Ichoku, R. C. Levy, R. G. Kleidman, T. F. Eck, E. Vermote, and B. N. Holben, 2005: The MODIS aerosol algorithm, products and validation, *J. Atmos. Sci.*, **62**: 947-973.

Sanford, T. B., P. G. Black, J. R. Haustein, J. W. Feeney, G. Z. Forristall, and J. F. Price, 1987: Ocean response to a hurricane, Part I: observations, *J. Phys. Oceanogr*., **17**, 2065–2083.

Shi, J. J., and Coauthors, 2010: WRF simulations of the 20–22 January 2007 snow events over eastern Canada: Comparison with in situ and satellite observations. *J. Appl. Meteor. Climatol.*, **49,** 2246–2266.

Stephens, G. L., N. B. Wood, and L. A. Pakula, 2004: On the radiative effects of dust on tropical convection, *Geophys. Res. Lett*., **31**: L23112, doi:10.1029/2004GL021342.

Sun, D., Z. Boybeyi, C. Yang, R. Yang, W. K. M. Lau, M. Kafatos, and G. Leptoukh, 2009: Numerical simulations of the impacts of the Saharan air layer on Atlantic tropical cyclone development. *J. Climate*, **22,** 6230**–**6250.

Tao, W.-K., and J. Simpson, 1993: The Goddard cumulus ensemble model. Part I: Model description. *Terr. Atmos. Oceanic Sci.*, **4**: 35–72.

Tao, W.-K,, J. Simpson, D. Baker, S. Braun, M.-D. Chou, B. Ferrier, D. Johnson, A. Khain, S. Lang, B. Lynn, C.-L. Shie, D. Starr, C.-H. Sui, Y. Wang, and P. Wetzel, 2003: Microphysics, radiation and surface processes in the Goddard Cumulus Ensemble (GCE) model. *Meteor. and Atmos. Phys.*, **82**: 97–137.

Thorncroft, C., and K. Hodges, 2001: African Easterly Wave Variability and Its Relationship to Atlantic Tropical Cyclone Activity. *J. Climate*, **14**: 1166–1179.

Tompkins, A. M., C. Cardinali, J.-J. Morcrette, and M. Rodwell, 2005: Influence of aerosol climatology on forecasts of the African easterly jet. *Geophys. Res. Lett.*, **32**, L10801, doi:10.1029/ 2004GL022189.

Volz, F., 1973: Infrared optical constants of ammonium sulfate, Sahara dust, volcanic pumice, and flyash. *Appl. Opt.*, **12**:564–568.

Wong, Sun, Andrew E. Dessler, Natalie M. Mahowald, Ping Yang, Qian Feng, 2009: Maintenance of Lower Tropospheric Temperature Inversion in the Saharan Air Layer by Dust and Dry Anomaly. *J. Climate*, **22**, 5149–5162.

World Climate Program, 1986: A preliminary cloudless standard atmosphere for radiation computation. WCP-112, WMO/ TD-24, 60 pp.

Zhang, H., G. M. McFarquhar, W. R. Cotton, and Y. Deng, 2009: Direct and indirect impacts of Saharan dust acting as cloud condensation nuclei on tropical cyclone eyewall development. *Geophys. Res. Lett.*, **36**, L06802. doi:10.1029/2009GL037276.

Zhao C, X Liu, LR Leung, and S Hagos, 2011. "Radiative impact of mineral dust on monsoon precipitation variability over West Africa." *Atmospheric Chemistry and Physics* 11(5):1879-1893. DOI: 10.5194/acp-11-1879-2011.

Zipser, E.J., C.H. Twohy, S.C. Tsay, K.L. Thornhill, S. Tanelli, R. Ross, T.N. Krishnamurti, Q. Ji, G. Jenkins, S. Ismail, N.C. Hsu, R. Hood, G.M. Heymsfield, A. Heymsfield, J. Halverson, H.M. Goodman, R. Ferrare, J.P. Dunion, M. Douglas, R. Cifelli, G. Chen, E.V. Browell, and B. Anderson, 2009: The Saharan Air Layer and the Fate of African Easterly Waves—NASA's AMMA Field Study of Tropical Cyclogenesis. *Bull. Amer. Meteor. Soc.*, **90**: 1137–1156.

List of Tables

List of Figures

Figure 1. Five-month (June-October) average (1) MODIS AOT (yellow shaded), and positive relative vorticity (contoured, unit: 10^{-5} s^{-1}) and winds (vector, unit: m s^{-1}) at 700 hPa (left column); (2) Temperature (color shaded, unit: K) and winds (vector, unit: m s^{-1}) at 700 hPa (middle column); and (3) Temperature (color shaded, unit: K) and winds (vector, unit: m s^{-1}) at 1000 hPa (right column) for years 2003 (top)-2007(bottom), respectively. Relative vorticity, winds, and temperature are obtained from ECMWF operational analysis.

Figure 2. Time series of ECMWF relative vorticity at 700 hPa (purple striped area encloses relative vorticity larger than 1.0×10^{-5} s^{-1}) and MODIS AOT (yellow shaded area), zonally averaged between 15°W and 50°W, in (a) 2003; (b) 2004; (c) 2005; (d) 2006; and (e) 2007. Red stars denote the dates and latitudes of TC-genesis identified by National Hurricane Center.

Figure 3. Composite of MODIS AOT (color shaded), and ECMWF relative vorticity (contour; interval = 0.5 x 10^{-5} s^{-1}) and winds (vector; unit: m s^{-1}) at 700 hPa for the 60 AEWs on (a) the day of; (b) 1 day after; (c) 2 days after; and (d) 3 days after, the AEWs leave the coast of African continent. The thick purple line denotes zero relative vorticity.

Figure 4. Aerosol-induced clear-sky instantaneous heating rate (unit: K/day) at 12:00 (local time). Dotted area denotes the location of the prescribed dust layer.

Figure 5. Domain-averaged time-height plot of temperature (K) difference between (a) WA_L and NA experiments; and (b) WA_H and NA experiments, averaged over 60 pairs of simulations. Dotted area denotes the location of the prescribed dust layer.

Figure 6. Time series of domain-averaged tropospheric stability difference (defined as potential temperature difference between 200 hPa and 1000 hPa) between 60 pairs of (a) WA_L and NA experiments; and (b) WA_H and NA experiments (unit: K).

Figure 7. Time series of domain-averaged 315 K potential vorticity difference between 60 pairs of (a) WA_L and NA experiments; and (b) WA_H and NA experiments (unit: PVU).

Figure 8. Histogram of eddy kinetic energy (unit: kJ/m^2) of 60 AEWs in (a) NA (solid fill) and WA_L (crosshatch) experiments, and (b) NA (solid fill) and WA_H (crosshatch) experiments.

Figure 9. Histogram of eddy kinetic energy increase (unit: percent) of the 60 AEWs due to aerosol radiative forcing at 700-850hPa (solid fill) and 600-850hPa (crosshatch).

	AEW disturbance	Dust outbreak	TC-genesis
2003	39	30	7
2004	36	27	6
2005	32	29	7
2006	37	27	3
2007	32	27	4

Table 1. Number of AEW disturbances, dust outbreaks, TC-genesis events in 2003, 2004, 2005, 2006, and 2007.

Case	Starting date		Case	Starting date		Case	Starting date		Case	Starting date
1	2003-08-06		16	2004-08-21		31	2005-08-22		46	2006-09-08
2	2003-08-13		17	2004-08-25		32	2005-08-27		47	2006-09-12
3	2003-08-17		18	2004-08-29		33	2005-08-30		48	2006-09-15
4	2003-08-22		19	2004-09-04		34	2005-09-04		49	2006-09-19
5	2003-08-25		20	2004-09-07		35	2005-09-07		50	2006-09-23
6	2003-08-29		21	2004-09-09		36	2005-09-13		51	2007-08-03
7	2003-09-01		22	2004-09-14		37	2005-09-21		52	2007-08-11
8	2003-09-06		23	2004-09-16		38	2006-08-03		53	2007-08-22
9	2003-09-11		24	2004-09-19		39	2006-08-06		54	2007-08-28
10	2003-09-22		25	2004-09-22		40	2006-08-12		55	2007-09-01
11	2003-09-24		26	2005-08-05		41	2006-08-18		56	2007-09-06
12	2004-08-01		27	2005-08-09		42	2006-08-21		57	2007-09-12
13	2004-08-05		28	2005-08-11		43	2006-08-25		58	2007-09-17
14	2004-08-12		29	2005-08-15		44	2006-08-29		59	2007-09-21
15	2004-08-18		30	2005-08-20		45	2006-09-01		60	2007-09-25

Table 2. List of the starting date of AEW cases.

τ^{sw}	$\omega_0{}^{sw}$	g^{sw}	τ^{lw}	$\omega_0{}^{lw}$	g^{lw}
1.0	0.96	0.7	0.5	0.2	0.4

Table 3. Aerosol radiative properties including optical depth in shortwave (τ^{sw}), single scattering albedo in shotwave ($\omega_0{}^{sw}$), asymmetry factor in shortwave (g^{sw}), optical depth in longwave (τ^{lw}), single scattering albedo in longwave ($\omega_0{}^{lw}$), and asymmetry factor in longwave (g^{lw}).

		Simulation		
		NA	WA_L	WA_H
Energy terms ($kJ\ m^{-2}$)	P_Z	30.5	27.3	29.1
	K_Z	183.3	182.2	185.6
	P_E	35.8	35.4	35.2
	K_E	126.6	133.9	133.0
Energy conversion rates ($W\ m^{-2}$)	C_Z	-0.081	-0.024	-0.031
	C_A	-0.007	-0.008	-0.008
	C_K	0.068	0.078	0.084
	C_{PK}	0.332	0.422	0.395
Diabatic heating terms ($W\ m^{-2}$)	H_Z^C	-0.012	0.046	0.015
	H_Z^R	-0.044	-0.082	-0.072
	H_Z^B	-0.008	-0.009	-0.007
	H_E^C	0.197	0.256	0.241
	H_E^R	0.090	0.033	0.043
	H_E^B	-0.005	-0.005	-0.005

Table 4. Energy terms, energy conversion rates, and diabatic heating terms averaged over 60 AEWs.

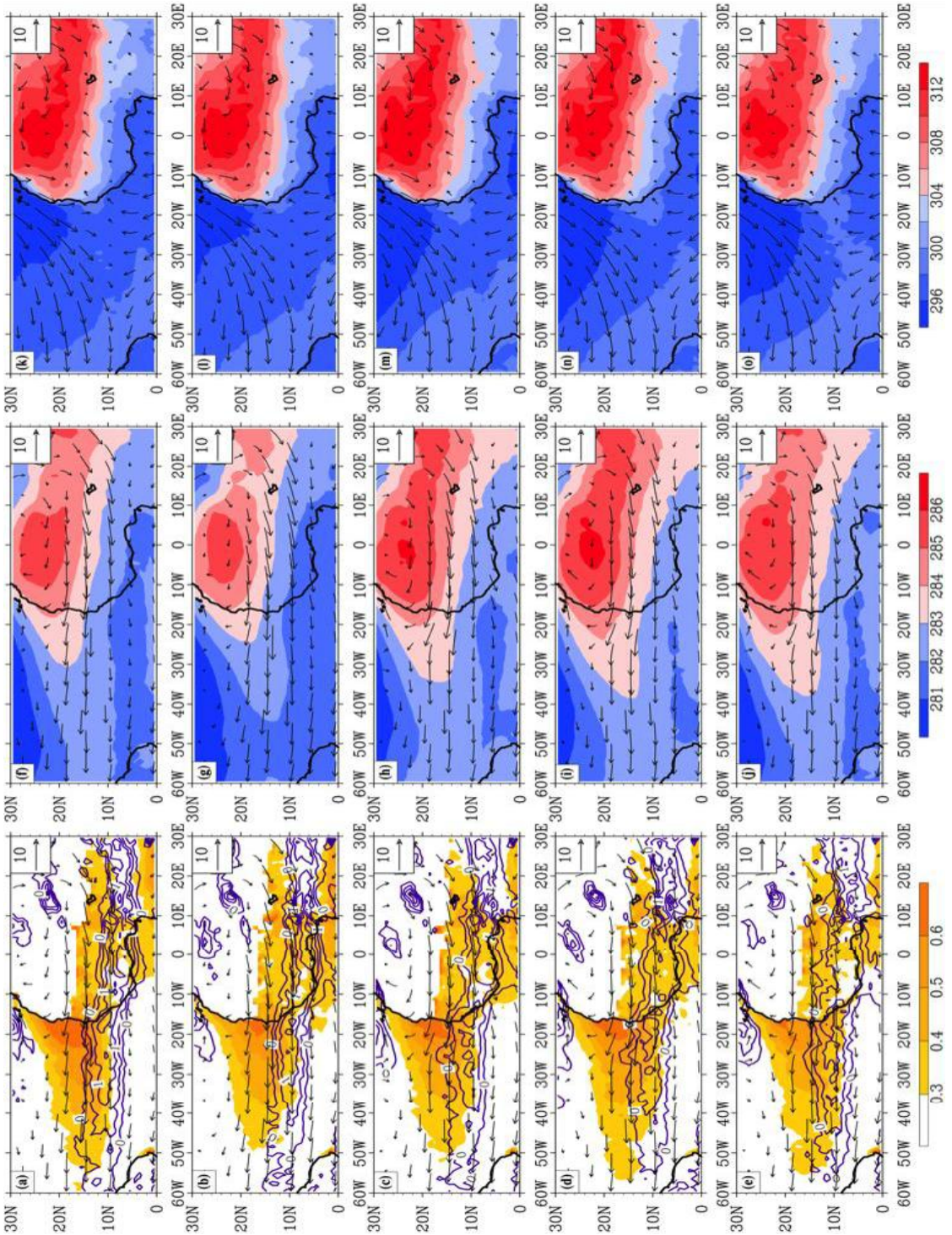

Figure 1. Five-month (June-October) average (1) MODIS AOT (yellow shaded), and positive relative vorticity (contoured, unit: 10^{-5} s^{-1}) and winds (vector, unit: m s^{-1}) at 700 hPa (left column); (2) Temperature (color shaded, unit: K) and winds (vector, unit: m s^{-1}) at 700 hPa (middle column); and (3) Temperature (color shaded, unit: K) and winds (vector, unit: m s^{-1}) at 1000 hPa (right column) for years 2003 (top)-2007(bottom), respectively. Relative vorticity, winds, and temperature are obtained from ECMWF operational analysis.

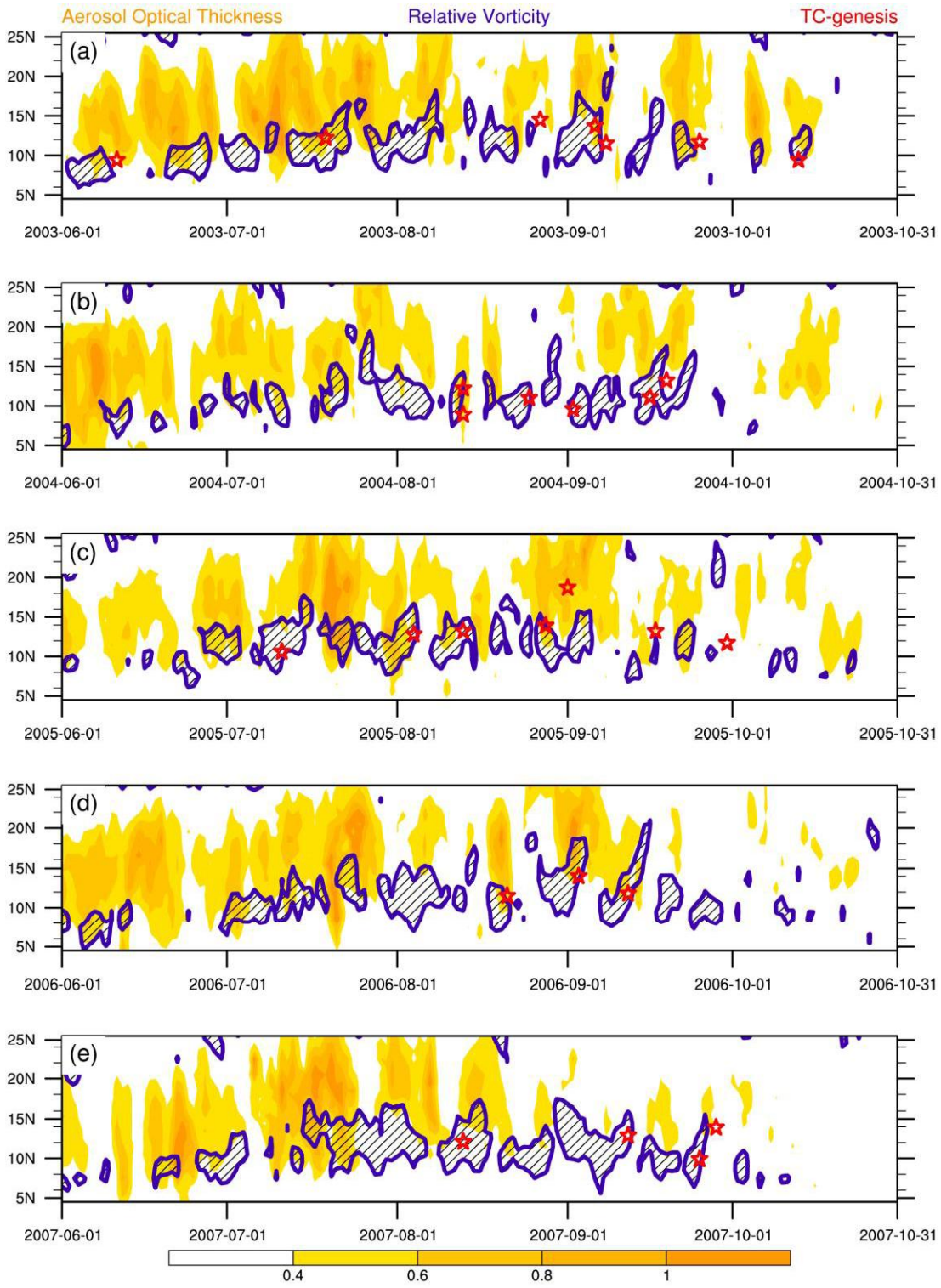

Figure 2. Time series of ECMWF relative vorticity at 700 hPa (purple striped area encloses relative vorticity larger than 1.0×10^{-5} s^{-1}) and MODIS AOT (yellow shaded area), zonally averaged between 15°W and 50°W, in (a) 2003; (b) 2004; (c) 2005; (d) 2006; and (e) 2007. Red stars denote the dates and latitudes of TC-genesis identified by National Hurricane Center.

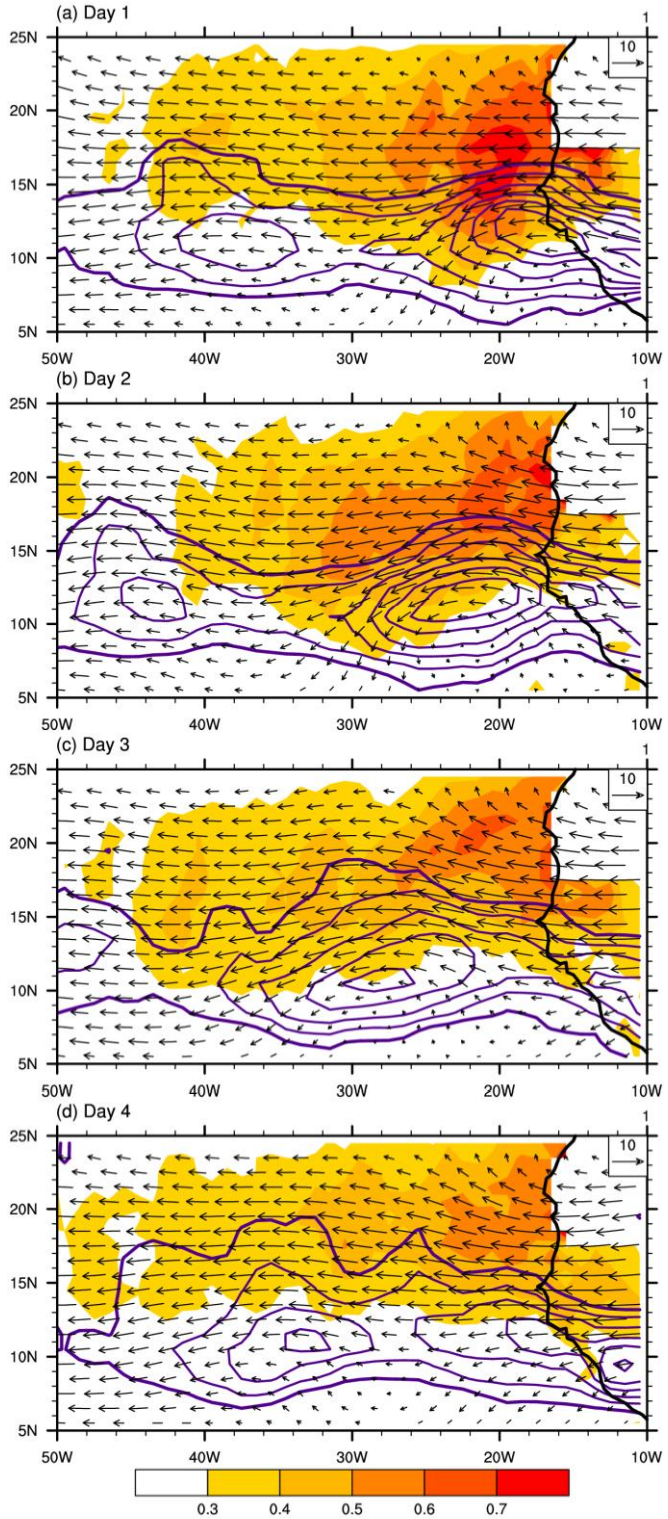

Figure 3. Composite of MODIS AOT (color shaded), and ECMWF relative vorticity (contour; interval = 0.5 x 10^{-5} s^{-1}) and winds (vector; unit: m s^{-1}) at 700 hPa for the 60 AEWs on (a) the day of; (b) 1 day after; (c) 2 days after; and (d) 3 days after, the AEWs leave the coast of African continent. The thick purple line denotes zero relative vorticity.

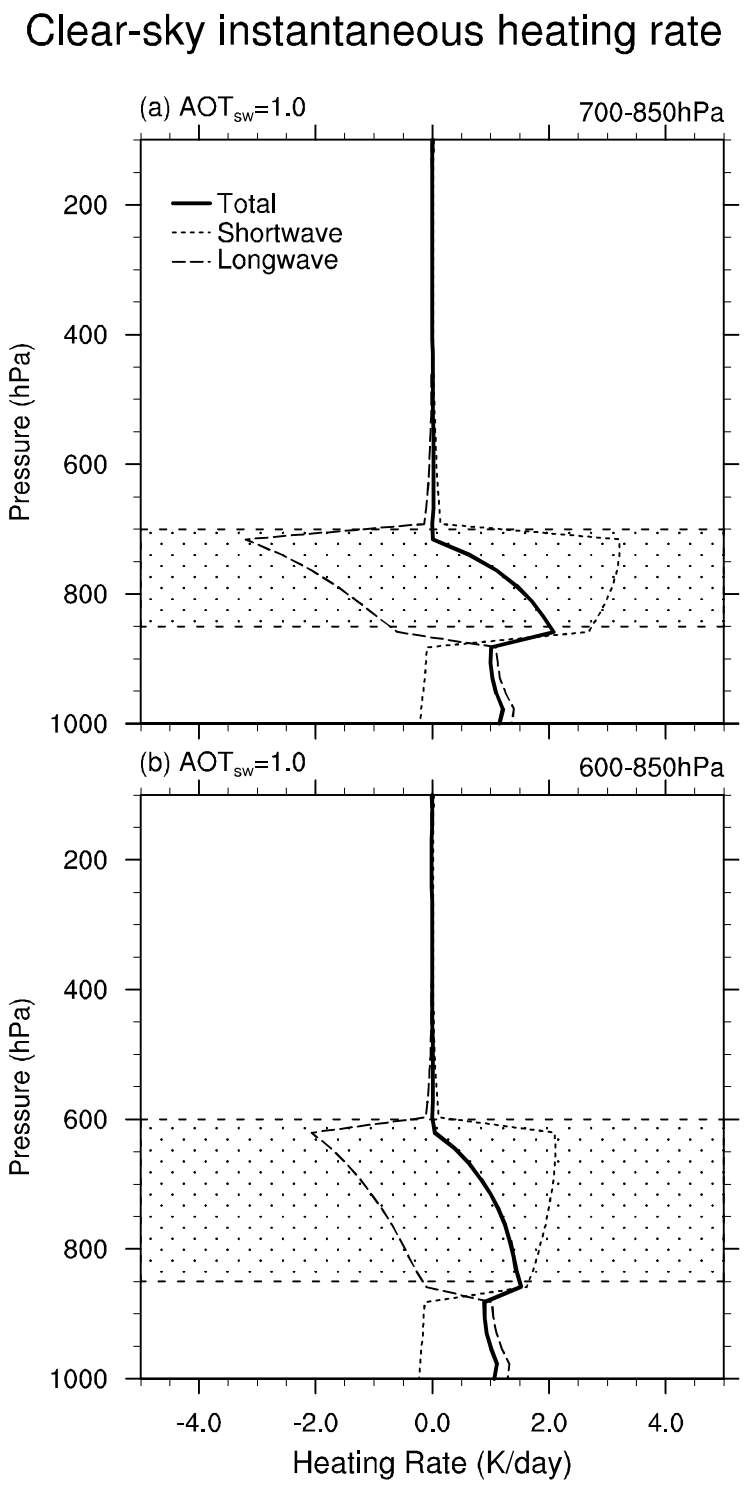

Figure 4. Aerosol-induced clear-sky instantaneous heating rate (unit: K/day) at 12:00 (local time). Dotted area denotes the location of the prescribed dust layer.

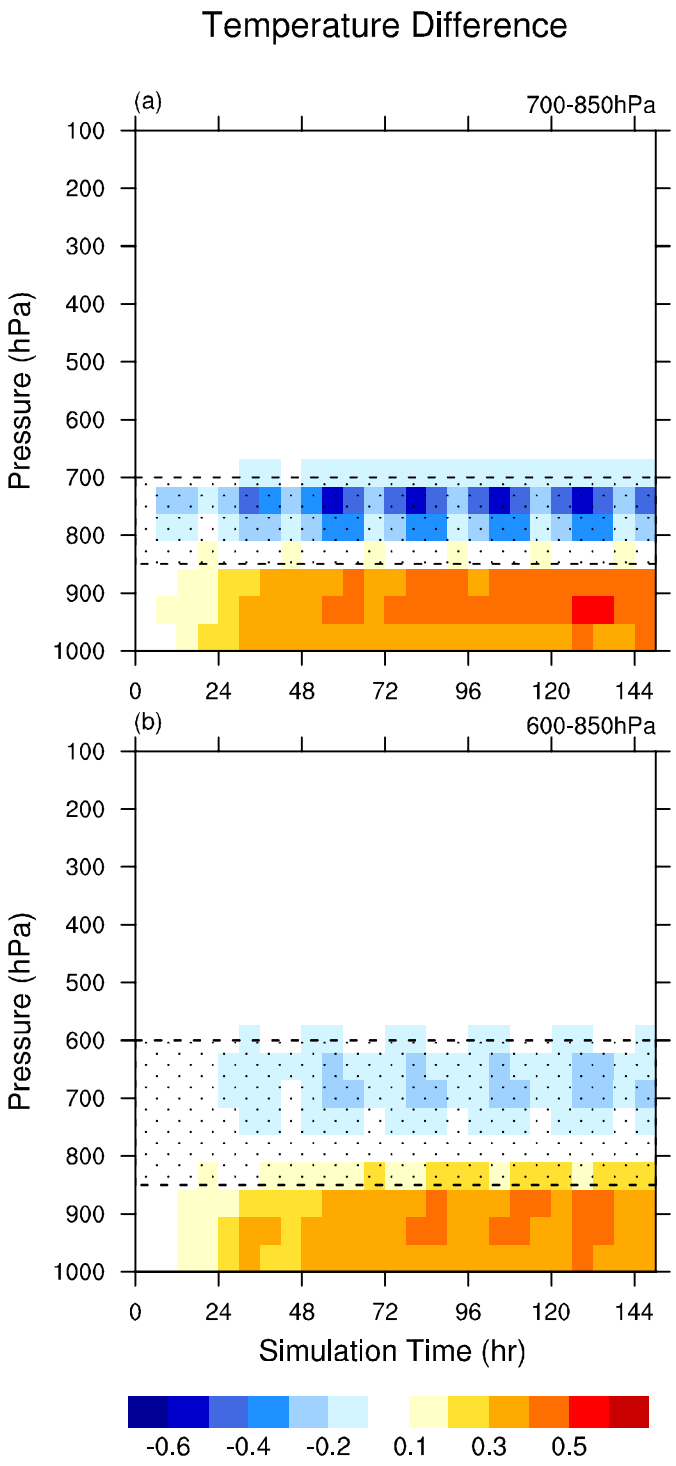

Figure 5. Domain-averaged time-height plot of temperature (K) difference between (a) WA_L and NA experiments; and (b) WA_H and NA experiments, averaged over 60 pairs of simulations. Dotted area denotes the location of the prescribed dust layer.

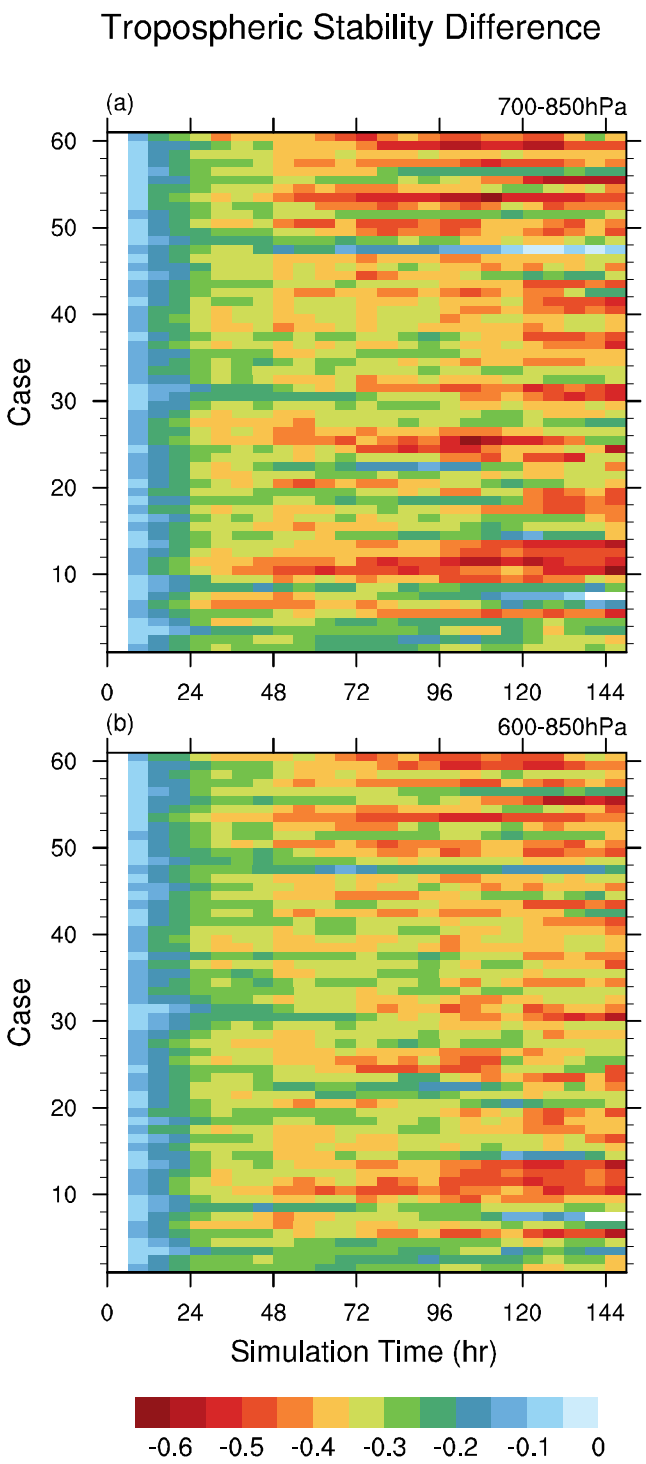

Figure 6. Time series of domain-averaged tropospheric stability difference (defined as potential temperature difference between 200 hPa and 1000 hPa) between 60 pairs of (a) WA_L and NA experiments; and (b) WA_H and NA experiments (unit: K).

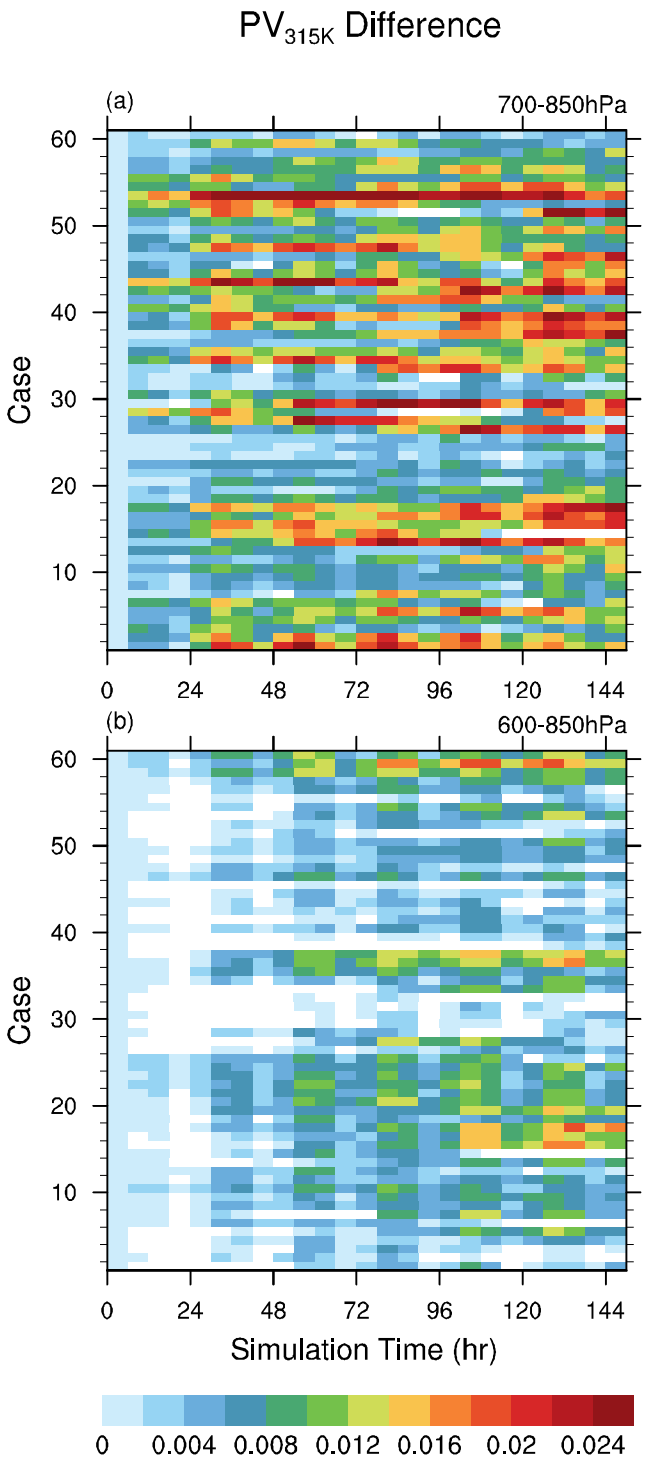

Figure 7. Time series of domain-averaged 315 K potential vorticity difference between 60 pairs of (a) WA_L and NA experiments; and (b) WA_H and NA experiments (unit: PVU).

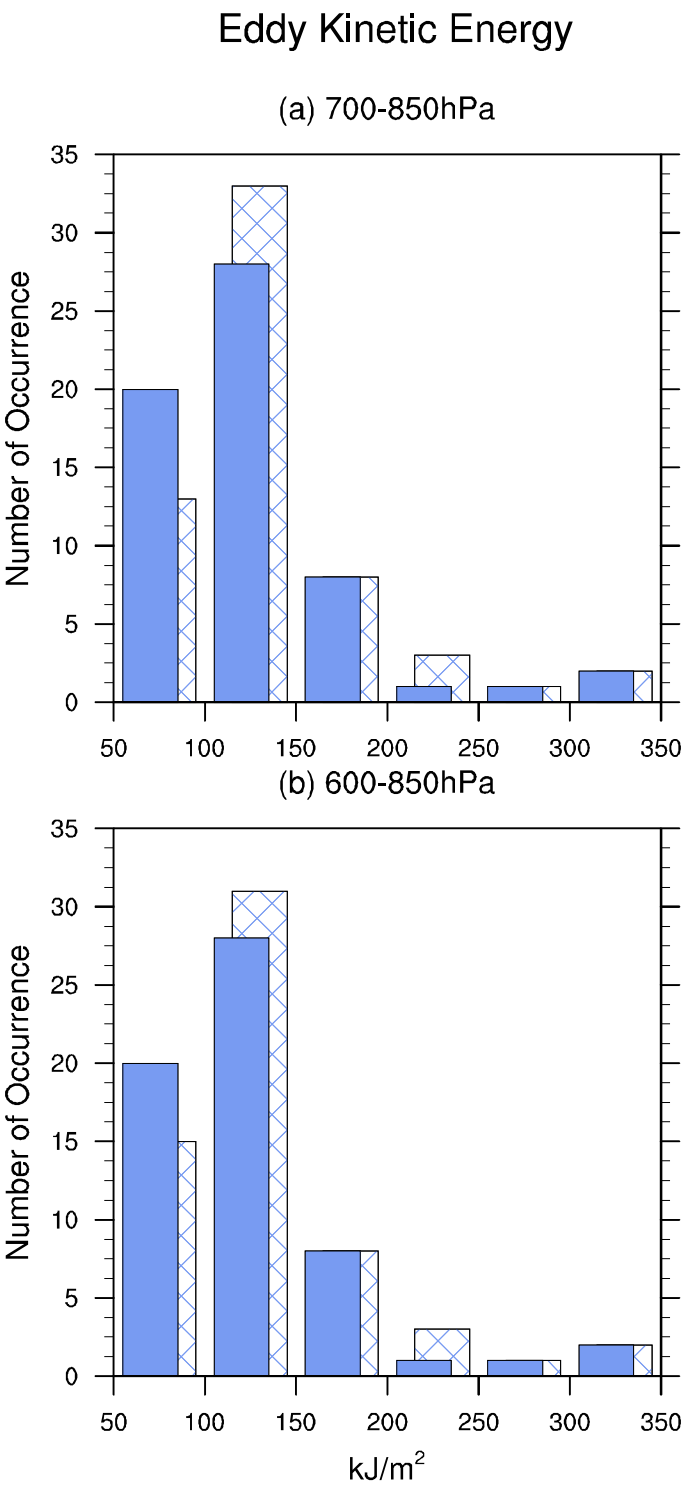

Figure 8. Histogram of eddy kinetic energy (unit: kJ/m^2) of 60 AEWs in (a) NA (solid fill) and WA_L (crosshatch) experiments, and (b) NA (solid fill) and WA_H (crosshatch) experiments.

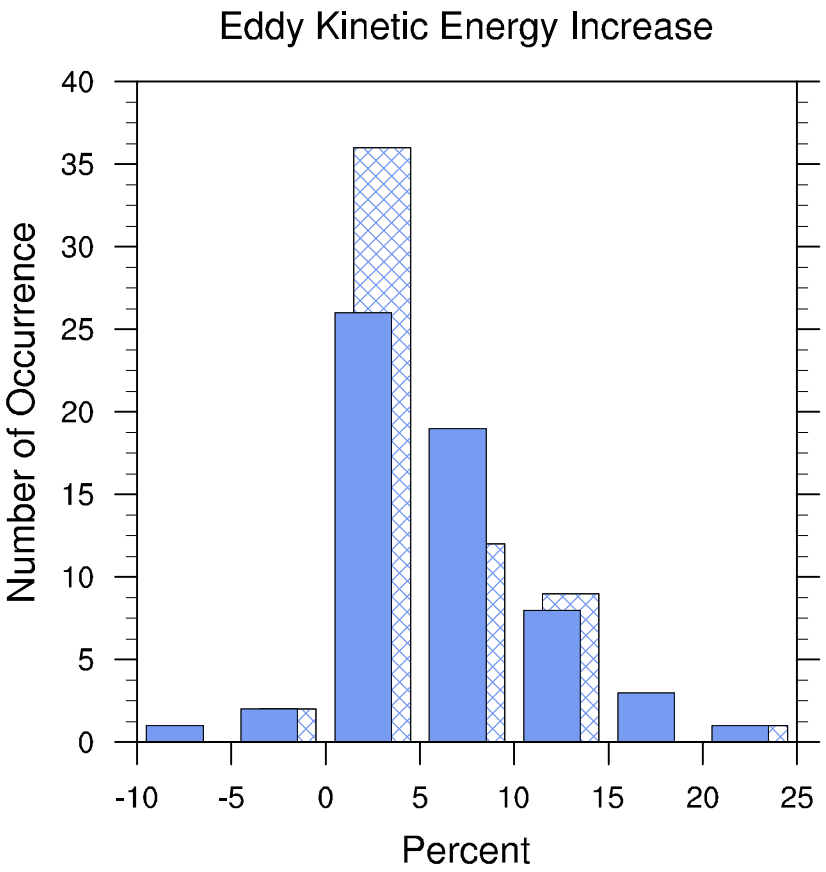

Figure 9. Histogram of eddy kinetic energy increase (unit: percent) of the 60 AEWs due to aerosol radiative forcing at 700-850hPa (solid fill) and 600-850hPa (crosshatch).